

Langmuir Films of Amphiphilic Crown Ethers

Paul A. Heiney,* MacKenzie R. Stetzer, and Oksana Y. Mindyuk

Department of Physics and Astronomy and Laboratory for Research on the Structure of Matter,
University of Pennsylvania, Philadelphia, Pennsylvania 19104

Elaine DiMasi

Physics Department, Brookhaven National Laboratory, Upton, New York 11973

Andrew R. McGhie

Laboratory for Research on the Structure of Matter, University of Pennsylvania,
Philadelphia, Pennsylvania 19104

Hu Liu and Amos B. Smith III*

Department of Chemistry and Laboratory for Research on the Structure of Matter,
University of Pennsylvania, Philadelphia, Pennsylvania 19104

Received: March 5, 1999; In Final Form: June 1, 1999

We have used X-ray reflectivity and grazing-incidence X-ray diffraction to study amphiphilic crown ethers **1** and **2** at the air–water interface. A new synthetic route was employed, which substantially reduced the level of impurities. Unlike previous studies of **1**, we saw no evidence of a first-order lying-down to standing-up transition of the alkyl tails. We did observe in both compounds a gradual reorientation of the tails away from the interface as the film was compressed, followed by an irreversible collapse to a multilayer structure. The monolayer films have a fluid-like inplane structure, while the multilayer films are crystalline.

1. Introduction

Langmuir films continue to attract attention both as model two-dimensional thermodynamic systems and for their potential applications. Grazing incidence diffraction (GID) and X-ray reflectivity (XR) have proven to be particularly useful structural probes and have shown that in model rodlike amphiphiles many different structures are possible, involving combinations of conformational rearrangements (chain melting, etc.), reorientation of the entire molecule (tilting transitions), and long-range cooperative effects. (See, e.g., refs 1 and 2 for reviews or ref 3 for a recent example.) Macrocyclic amphiphiles^{4,5} present a different set of issues. Such molecules are often capable of complexation with metal and molecular ions and are particularly interesting candidates as components of supramolecular ionic devices. Structural transitions in alkyl-substituted azacrowns and similar molecules have been associated either with rearrangements from flattened arrangements (with the macrocycle core cofacial with the water surface) to edge-on arrangements or with layering transitions.^{6–12}

Disubstituted crown ethers such as **1** (Figure 1) are in some ways intermediate between rodlike and macrocyclic amphiphiles, in that they possess both a macrocyclic core capable of complexation with metal ions and also two long chains that might be expected to behave individually like traditional rodlike amphiphiles.

Wei *et al.*^{13–18} studied **1** (as prepared by Xie *et al.*¹⁹) at the air–water interface and reported pressure–area (Π – A) isotherms with a stepped structure, with an initial rise from Π

= 0 to 27 mN/m at approximately 240 Å²/molecule, a horizontal plateau, and then a second sharp rise below 76 Å², leading to collapse at 65 mN/m. These features were explained as arising from a first-order transition from a lying-down configuration, with the central core and carbonyl groups in contact with the water subphase but the chains extending away from the subphase (as in Figure 1b), to a condensed phase with the alkyl chains and carbonyl groups directed away from the interface (Figure 1c). They also reported that monolayer Langmuir–Blodgett films of **1** could be used as alignment layers for liquid crystals.^{14–18} If the films were deposited with low spreading pressure, they obtained homogeneous alignment of the liquid crystal, while with high spreading pressure (presumably the conformation in Figure 1c) homeotropic alignment was obtained. Wei *et al.* inferred that the differing tail conformations in the Langmuir film were transferred to the solid substrate and provided a basis for an altered interaction with the liquid crystal molecules.

We were interested in further investigating the lying-down to standing-up transition in **1** using the greatly increased structural sensitivity made possible by X-ray scattering techniques. Accordingly, we prepared a sample using the synthetic sequence of Xie *et al.*,¹⁹ as outlined in Scheme 1. In our hands, however, the reaction between 4-(heptyloxy)benzoic chloride (**3**) and 4-hydroxybenzoic acid (**4**) gave a 70:16:14 mixture consisting of the desired 4-[(4-(heptyloxy)benzyl)oxy]benzoic acid (**5**), trimeric acid **6**, and 4-(heptyloxy)benzoic acid (**7**). Although acid **7** could be readily removed from **5** and **6** by column chromatography, the mixture of **5** and **6** proved inseparable either by fractional precipitation or column chro-

* To whom correspondence should be addressed.

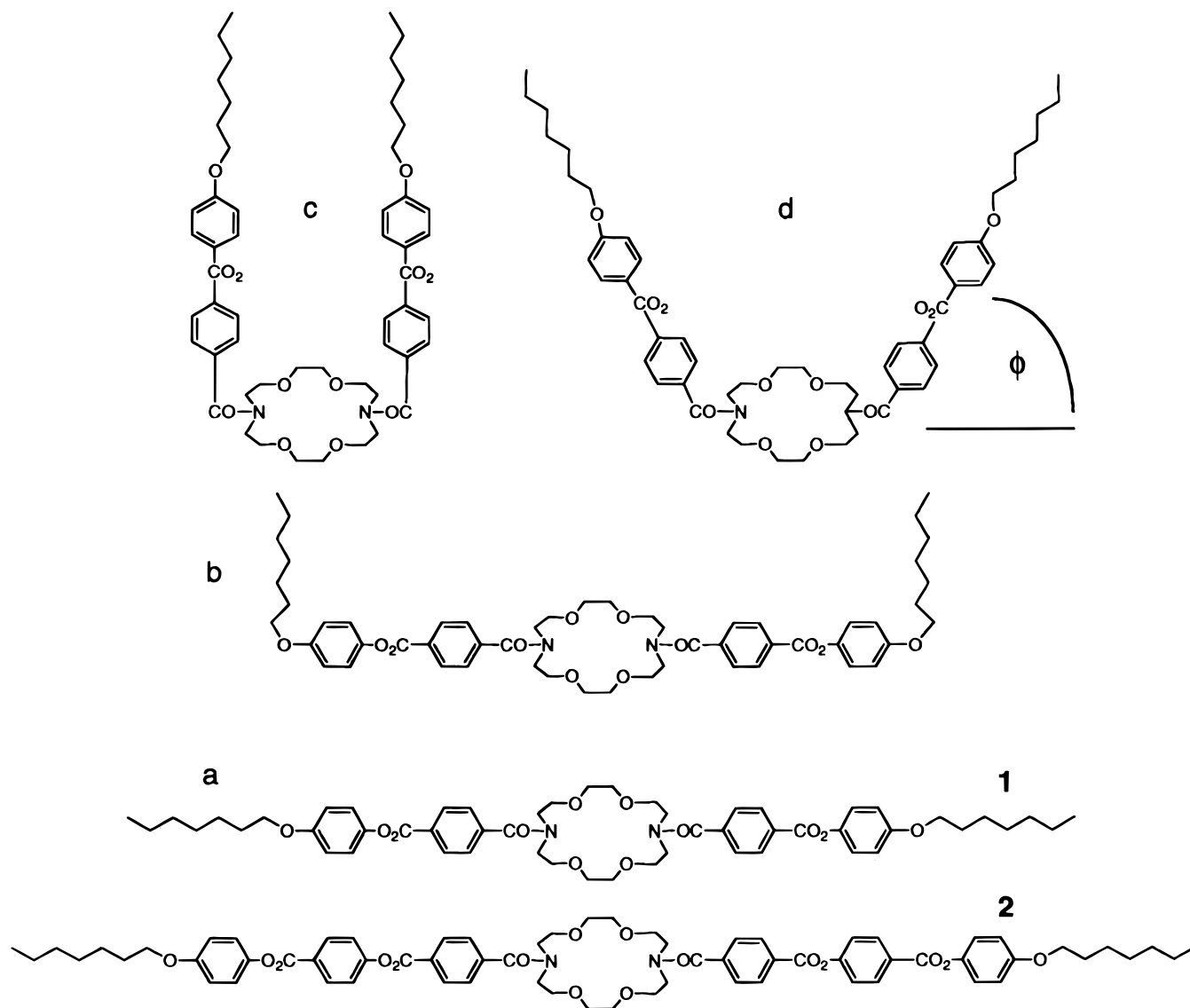


Figure 1. Structures of compounds **1** and **2** and some possible conformations of **1** at the air–water interface, drawn schematically: (a) crown ether core cofacial with water, phenyl rings, and alkyl chains in contact with water; (b) core and phenyl rings in contact with water, alkyl chains projecting away from the interface; (c) core in contact with water, phenyl rings and alkyl chains projecting directly away from water; (d) core in contact with water, phenyl rings and alkyl chains making an angle ϕ with the interface.

matography. All attempts to suppress the formation of **6** and **7** by modifying the reaction conditions failed. Notwithstanding this difficulty, the mixture of **5** and **6** was converted to a mixture of acid chlorides with thionyl chloride and then treated with diaza-18-crown-6-ether **8** to furnish crown ether liquid crystal **1**, which was contaminated as expected with corresponding unsymmetrical crown ether **9**. We were again unable to purify **1**. It is important to note that the ratio of **1** and **9** was not significantly altered by repeated fractional precipitation from ethanol, which is the purification method described by Xie *et al.*¹⁹ Furthermore, the Π – A isotherms we obtained using our (impure) sample of **1** were inconsistent with those previously reported.^{13–18}

We thus turned to an alternative synthetic route for the preparation of pure acid **5**, and in turn pure crown ether liquid crystal **1** (Scheme 2).

Toward this end, treatment of 4-hydroxybenzoic acid (**4**) with *N,N*-dimethylformamide di-*tert*-butyl acetal furnished *tert*-butyl 4-hydroxybenzoate (**10**) in 52% yield,²⁰ which was then converted to *tert*-butyl ester **11** in 89% yield upon treatment with 4-(heptyloxy)benzoic chloride (**3**). Acidic hydrolysis with

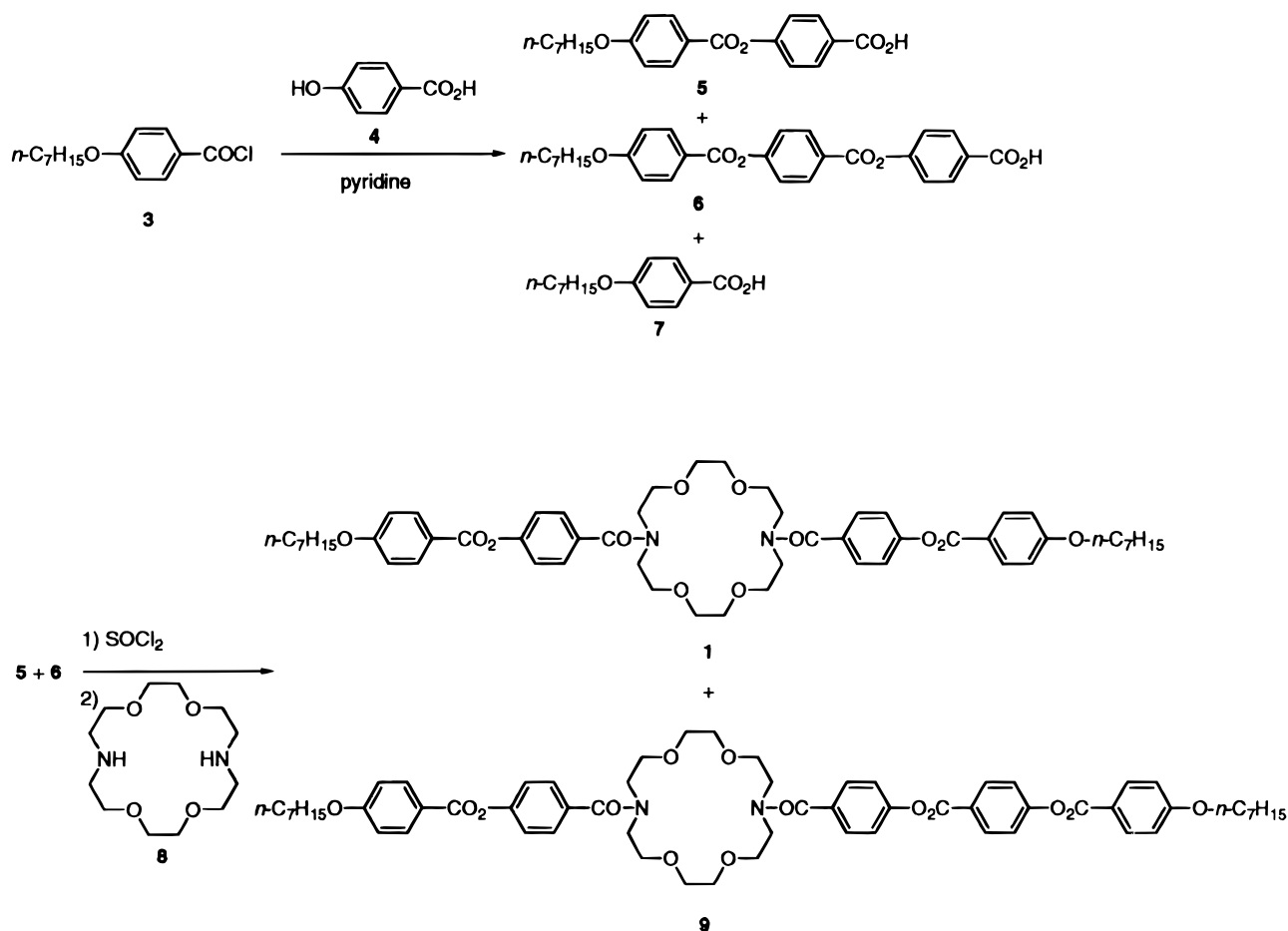
trifluoroacetic acid in the presence of anisole to capture the transient tertiary butyl carbocation afforded acid **5** in 74% yield without contamination. Formation of the corresponding acid chloride, followed by reaction with diaza-18-crown-6-ether **8** according to the reported procedure¹⁹ gave pure **1** in 68% yield. Crown ether liquid crystal **2** was prepared in a similar fashion (Scheme 3).

We then used Π – A isotherms, XR, and GID to study the pure samples of **1** and **2** thus obtained. We did not see the same behavior at the air–water interface as the Wei group, but we did see evidence of multilayer formation and collapse, as well as intralayer self-organization at higher pressures. In the remaining sections of this paper we will describe in more detail the synthesis of pure **1** and **2**, and the results of our physical measurements on these samples.

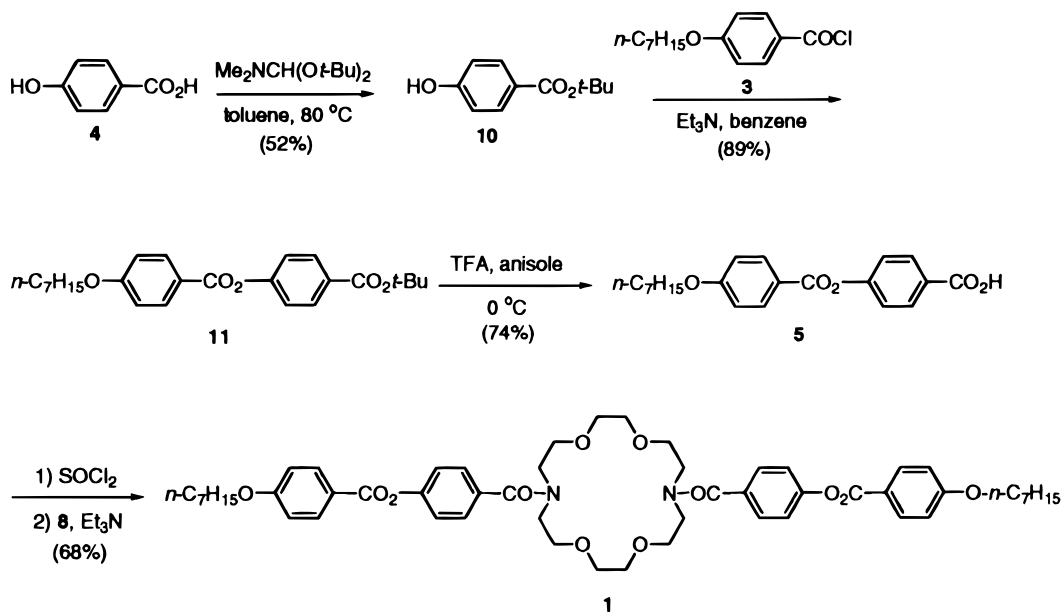
2. Experimental Section

Synthesis.²² *tert*-Butyl Ester **10**. A solution of 4-hydroxybenzoic acid (**4**, 1.58 g, 11.44 mmol) in anhydrous toluene (35 mL) was heated to 80 °C and dimethylformamide di-*tert*-butyl

SCHEME 1



SCHEME 2

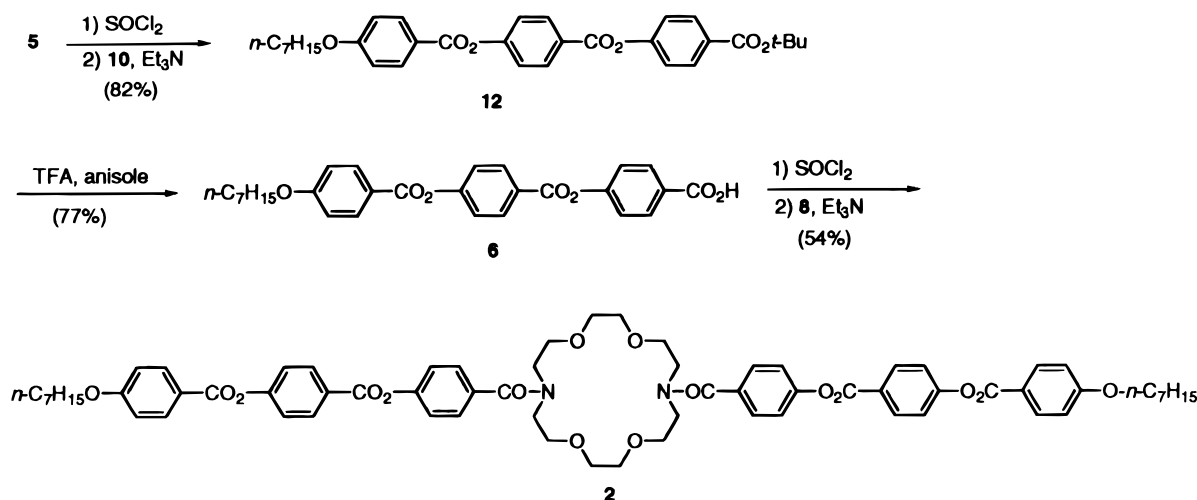


acetal (3.48 g, 22.88 mmol) added slowly. After 4 h, the reaction mixture was cooled to room temperature, diluted with brine (10 mL), and extracted with ethyl acetate (3 \times 20 mL). The combined organic extracts were washed with brine (2 \times 10 mL), dried over MgSO_4 , filtered, and concentrated. Flash chromatography (ethyl acetate/hexane, 20:80) provided **10** (1.15 g, 52% yield) as a white solid: mp 129–131 $^\circ\text{C}$ [lit.²⁰ mp 129–131

$^\circ\text{C}$]. The spectral properties of **10** were identical with literature values.²⁰

tert-Butyl Ester 11. A solution of ester **10** (0.39 g, 1.99 mmol) in anhydrous benzene (11 mL) was cooled to 0 $^\circ\text{C}$. Triethylamine (0.81 g, 8.0 mmol) was added followed by 4-(heptyloxy)benzoic chloride (**3**, 0.71 g, 2.79 mmol). The reaction was stirred at room temperature for 12 h and then concentrated. Flash

SCHEME 3



chromatography (ethyl acetate/hexane, 3:97) provided **11** (0.73 g, 89% yield) as a white solid: mp 94–95 °C; IR (KBr) 2960 (m), 1740 (s), 1710 (s), 1610 (s) cm^{-1} ; ^1H NMR (500 MHz, CDCl_3) δ 8.12 (d, J = 6.8 Hz, 2H), 8.04 (d, J = 6.7 Hz, 2H), 7.24 (d, J = 6.8 Hz, 2H), 6.95 (d, J = 6.9 Hz, 2H), 4.03 (t, J = 6.6 Hz, 2H), 1.84–1.77 (m, 2H), 1.59 (s, 9H), 1.49–1.42 (m, 2H), 1.39–1.28 (m, 6H), 0.89 (t, J = 6.9 Hz, 3H); ^{13}C NMR (500 MHz, CDCl_3) δ 165.1, 164.4, 163.7, 154.5, 132.4, 131.0, 129.5, 121.6, 121.2, 114.4, 81.1, 68.4, 31.8, 29.1, 29.0, 28.2, 25.9, 22.6, 14.1; high-resolution mass spectrum (FAB, NBA) m/z 413.2326 [(M + H) $^+$], calcd for $\text{C}_{25}\text{H}_{33}\text{O}_5$ 413.2328]. Anal. Calcd for $\text{C}_{25}\text{H}_{32}\text{O}_5$: C, 72.79; H, 7.82. Found: C, 73.02; H, 8.08.

Acid 5. A solution of *tert*-butyl ester **11** (0.20 g, 0.49 mmol) in methylene chloride (10 mL) at 0 °C was treated with anisole (1 mL) followed by trifluoroacetic acid (2.5 mL). The reaction mixture was stirred for 3 h and then concentrated. Flash chromatography (methanol/chloroform, 5:95) provided **5** (0.13 g, 74% yield) as a white solid: mp 156–160 °C; IR (KBr) 1740 (s), 1690 (s), 1610 (s) cm^{-1} ; ^1H NMR (500 MHz, CDCl_3) δ 8.18 (d, J = 8.8 Hz, 2H), 8.13 (d, J = 8.9 Hz, 2H), 7.33 (d, J = 8.7 Hz, 2H), 6.97 (d, J = 8.8 Hz, 2H), 4.04 (t, J = 6.6 Hz, 2H), 1.86–1.78 (m, 2H), 1.49–1.44 (m, 2H), 1.41–1.28 (m, 6H), 0.89 (t, J = 6.9 Hz, 3H); ^{13}C NMR (500 MHz, CDCl_3) δ 169.6, 164.3, 163.9, 155.5, 132.4, 131.9, 126.5; 122.0, 121.0, 114.4, 68.4, 31.8, 29.1, 29.0, 26.0, 22.6, 14.1; high-resolution mass spectrum (FAB, NBA) m/z 357.1697 [(M + H) $^+$], calcd for $\text{C}_{21}\text{H}_{25}\text{O}_5$ 357.1702]. Anal. Calcd for $\text{C}_{21}\text{H}_{24}\text{O}_5$: C, 70.77; H, 6.79. Found: C, 70.82; H, 6.88.

Crown Ether Liquid Crystal 1. A solution of acid **5** (0.127 g, 0.357 mmol) in thionyl chloride (neat, 4 mL) was heated to reflux under argon for 16 h. The reaction was then cooled to room temperature, concentrated, and diluted with anhydrous benzene (3 mL). The resultant mixture was treated with a solution of crown ether **8** (0.043 g, 0.162 mmol) and triethylamine (0.073 g, 0.714 mmol) in anhydrous benzene (5 mL) and then stirred at room temperature for 50 min, heated to reflux for 16 h, cooled to room temperature, and concentrated. Flash chromatography (methanol/chloroform, 3:97) afforded **1** (0.133 g, 88% yield) as a white solid, which was recrystallized twice from ethanol to give **1** (0.103 g, 68% yield) as a white solid: mp 125–128 °C; IR (KBr) 1740 (s), 1640 (s), 1610 (s) cm^{-1} ; ^1H NMR (500 MHz, CDCl_3) δ 8.10 (d, J = 8.8 Hz, 4H), 7.44 (d, J = 8.4 Hz, 4H), 7.22 (d, J = 8.4 Hz, 4H), 6.95 (d, J = 8.9 Hz, 4H), 4.02 (t, J = 6.6 Hz, 4H), 3.84–3.45 (m, 24H), 1.83–

1.76 (m, 4H), 1.49–1.42 (m, 4H), 1.39–1.24 (m, 12H), 0.88 (t, J = 6.9 Hz, 6H); ^{13}C NMR (500 MHz, CDCl_3) δ 171.5, 164.6, 163.7, 151.8, 134.1, 132.3, 128.1, 121.8, 121.3, 114.4, 70.7, 69.8, 68.4, 50.1, 46.4, 31.7, 29.1, 29.0, 25.9, 22.6, 14.0; high-resolution mass spectrum (FAB, NBA) m/z 961.4821 [(M + Na) $^+$], calcd for $\text{C}_{54}\text{H}_{70}\text{N}_2\text{O}_{12}\text{Na}$ 961.4826]. Anal. Calcd for $\text{C}_{54}\text{H}_{70}\text{N}_2\text{O}_{12}$: C, 69.06; H, 7.51; N, 2.98. Found: C, 68.97; H, 7.55; N, 2.86.

***tert*-Butyl Ester 12.** A solution of acid **5** (0.130 g, 0.365 mmol) in thionyl chloride (neat, 4 mL) was heated to reflux under argon for 5 h. The reaction was then cooled to room temperature, concentrated, diluted with anhydrous benzene (5 mL), and cooled to 0 °C. The resultant mixture was then treated with a solution of *tert*-butyl ester **10** (0.071 g, 0.365 mmol) and triethylamine (0.146 g, 1.46 mmol) in anhydrous benzene (3 mL), warmed to room temperature, stirred for 16 h, and concentrated. Flash chromatography (ethyl acetate/hexane, 5:95) afforded **12** (0.159 g, 82% yield) as a white solid: mp 127–130 °C (dec); IR (KBr) 2960 (m), 1750 (s), 1720 (m), 1610 (s) cm^{-1} ; ^1H NMR (500 MHz, CDCl_3) δ 8.28 (d, J = 8.8 Hz, 2H), 8.15 (d, J = 8.9 Hz, 2H), 8.08 (d, J = 8.7 Hz, 2H), 7.38 (d, J = 8.7 Hz, 2H), 7.28 (d, J = 8.8 Hz, 2H), 6.99 (d, J = 9.0 Hz, 2H), 4.06 (t, J = 6.5 Hz, 2H), 1.84–1.81 (m, 2H), 1.61 (s, 9H), 1.52–1.46 (m, 2H), 1.41–1.29 (m, 6H), 0.91 (t, J = 7.0 Hz, 3H); ^{13}C NMR (500 MHz, CDCl_3) δ 165.0, 164.3, 164.0, 163.9, 155.6, 154.2, 132.4, 131.9, 131.0, 129.8, 126.6, 122.2, 121.5, 121.0, 114.5, 81.2, 68.4, 31.8, 29.1, 29.0, 28.2, 26.0, 22.6, 14.1; high-resolution mass spectrum (FAB, NBA) m/z 555.2362 [(M + Na) $^+$], calcd for $\text{C}_{32}\text{H}_{36}\text{O}_7\text{Na}$ 555.2359]. Anal. Calcd for $\text{C}_{32}\text{H}_{36}\text{O}_7$: C, 72.16; H, 6.81. Found: C, 72.52; H, 6.74.

Acid 6. A solution of *tert*-butyl ester **12** (0.140 g, 0.263 mmol) in methylene chloride (10 mL) was treated with anisole (1 mL) followed by trifluoroacetic acid (2.5 mL). The reaction mixture was stirred for 3 h and then concentrated. The resultant solid was washed with ethyl ether (3 \times 6 mL) and filtered to give **6** (0.096 g, 77% yield) as a white solid: mp 220–225 °C; IR (KBr) 2960 (m), 1750 (s), 1700 (s), 1610 (s) cm^{-1} ; ^1H NMR (500 MHz, $\text{DMF}-d_7$) δ 8.32 (d, J = 8.8 Hz, 2H), 8.17 (d, J = 8.9 Hz, 2H), 8.16 (d, J = 8.6 Hz, 2H), 7.62 (d, J = 8.8 Hz, 2H), 7.55 (d, J = 8.7 Hz, 2H), 7.20 (d, J = 9.0 Hz, 2H), 4.18 (t, J = 6.5 Hz, 2H), 1.84–1.80 (m, 2H), 1.50–1.27 (m, 8H), 0.89 (t, J = 7.1 Hz, 3H); ^{13}C NMR (500 MHz, $\text{DMF}-d_7$) δ 167.4, 164.7, 164.6, 164.5, 156.4, 155.2, 132.9, 132.3, 131.7, 129.7, 127.3, 123.4, 122.9, 121.5, 115.5, 69.0, 32.3, 29.6, 29.5, 26.4, 23.0, 14.2; high-resolution mass spectrum (FAB, NBA)

m/z 477.1904 $[(M + H)^+]$; calcd for $C_{28}H_{29}O_7$ 477.1913]. Anal. Calcd for $C_{28}H_{28}O_7$: C, 70.57; H, 5.92. Found: C, 70.44; H, 5.93.

Crown Ether Liquid Crystal 2. A solution of acid **6** (0.056 g, 0.118 mmol) in thionyl chloride (neat, 3 mL) was heated to reflux under argon for 5 h. The reaction was then cooled to room temperature, concentrated, diluted with anhydrous benzene (2 mL), and cooled to 0 °C. The resultant mixture was then treated with a solution of crown ether **8** (0.014 g, 0.05 mmol) and triethylamine (0.024 g, 0.24 mmol) in anhydrous benzene (2 mL), warmed to room temperature, stirred for 16 h, and concentrated. Flash chromatography (methanol/chloroform, 5:95) afforded **2** (0.049 g, 78% yield) as a white solid, which was recrystallized twice from ethanol to give **2** (0.034 g, 54% yield) as a white solid: mp 192–193 °C; IR (KBr) 2750 (m), 1750 (s), 1620 (s) cm^{-1} ; 1H NMR (500 MHz, $CDCl_3$) δ 8.25 (d, J = 8.6 Hz, 4H), 8.13 (d, J = 8.9 Hz, 4H), 7.47 (d, J = 8.0 Hz, 4H), 7.35 (d, J = 8.6 Hz, 4H), 7.25 (d, J = 8.3 Hz, 4H), 6.96 (d, J = 8.9 Hz, 4H), 4.04 (t, J = 6.6 Hz, 4H), 3.84–3.48 (m, 24H), 1.84–1.78 (m, 4H), 1.49–1.42 (m, 4H), 1.39–1.29 (m, 12H), 0.89 (t, J = 7.1 Hz, 6H); ^{13}C NMR (500 MHz, $CDCl_3$) δ 171.4, 164.3, 164.1, 163.9, 155.6, 151.6, 134.4, 132.4, 131.8, 128.2, 126.6, 122.2, 121.8, 121.0, 114.5, 70.7, 69.8, 68.4, 50.1, 46.4, 31.7, 29.1, 28.9, 25.9, 22.6, 14.0; high-resolution mass spectrum (FAB, NBA) m/z 1201.5291 $[(M + Na)^+]$; calcd for $C_{68}H_{78}N_2O_{16}Na$ 1201.5249]. Anal. Calcd for $C_{68}H_{78}N_2O_{16}$: C, 69.25; H, 6.67; N, 2.38. Found: C, 68.85; H, 6.33; N, 2.05.

Calorimetry. Differential scanning calorimetry (DSC) measurements employed a TA Instruments DSC 2920 calorimeter. The samples were loaded in air into crimped Al DSC pans, and the measurements were made under flowing He.

X-ray Scattering. X-ray measurements were conducted at beam line X22B (λ = 1.55 Å) of the National Synchrotron Light Source, Brookhaven National Laboratory, using a liquid surface spectrometer as described previously.^{10,21,23,24} X-ray measurements on **1** were conducted at 291 K, and those on **2** at 293 K, unless otherwise indicated.

A monochromatic X-ray beam was deflected toward the water surface via Bragg reflection from a Ge(111) crystal. For XR measurements, the momentum transfer is normal to the interface (in the Q_z direction). In this case the instrumental resolution was determined primarily by the slits between the sample and the detector. These slits were always set to optimize the resolution in the scattering plane while increasing the signal by lowering the resolution out of the scattering plane. The resolution in the direction perpendicular to the water surface (Q_z) during XR measurements was 0.008 Å⁻¹. For GID measurements, the incident beam was almost parallel to the water surface and the scattered photons were collected with a Braun position sensitive direction oriented with the wire in the vertical direction. The resolution in the Q_{xy} scattering plane was set by the incoming slits to be approximately 0.007 Å⁻¹.

Pressure–Area Isotherms. All subphases employed water purified using a Millipore filtration system with a resulting resistivity ρ > 18 MΩ/cm. Small quantities of solute ($\approx 10^{-3}$ g) were weighed on a Denver Instruments A-200DS balance to an accuracy of 10^{-4} g, giving a typical mass uncertainty of 3–5%. All monolayers were spread from 10^{-3} to 10^{-4} M chloroform solutions. The Langmuir trough was cleaned between experiments using a hexane rinse followed by an ethanol rinse and three rinses with clean H₂O. Initial pressure–area isotherms, including those shown in Figure 3, were collected on a commercially available Lauda film balance using the movable barrier/Langmuir float technique. To verify that our

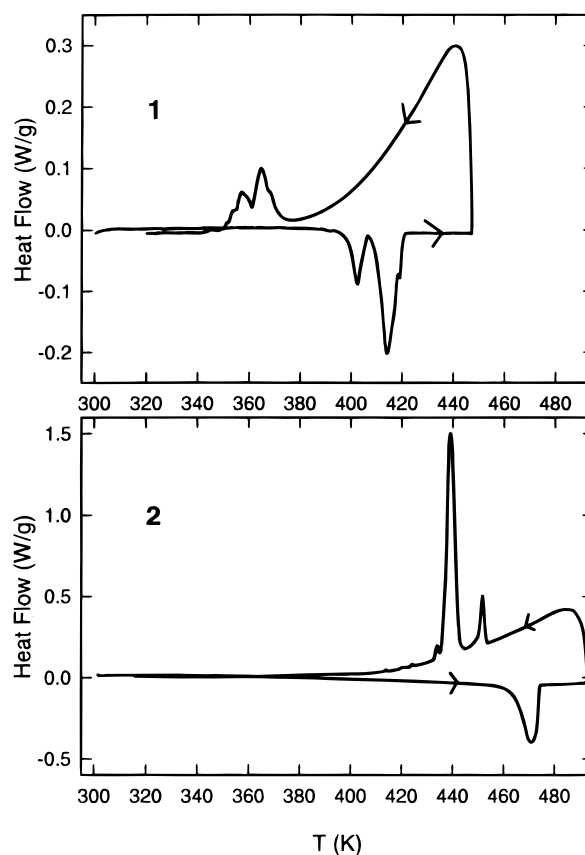


Figure 2. Differential scanning calorimetry data for **1** (top) and **2** (bottom). Data were collected at a scan rate of 2 K/min in He.

results were not affected by incomplete mixing of the sample with the solvent, selected solutions were sonicated before deposition, without producing any qualitative change from the isotherms shown in Figure 3. X-ray measurements employed a movable barrier/Langmuir float trough, as previously described.^{10,21,23} Pressure–area isotherms were remeasured for each compound immediately prior to the scattering measurements. Subsequently, a new film was deposited and compressed to the desired pressure. Except as otherwise indicated, the spreading pressure decreased by less than 10% during the course of an X-ray measurement. The combined uncertainty in molecular area (due to measurement and deposition error and pressure variation during the measurement) was on the order of 10%. It is worth noting that the isotherms measured on the two troughs were consistent to within 10% in pressure and area even though the source of water for the subphases was different.

3. Results

Figure 2 shows characteristic DSC data for **1** and **2**. Xie *et al.* previously reported¹⁹ a nematic liquid crystal phase in **1** between 393 and 408 K, as observed by DSC and optical microscopy. Similarly, we observed two endotherms upon heating **1**, with onsets at 399 and 410 K, and two related exotherms at low temperatures upon cooling. Optical microscopy under crossed polarizers showed that the region between the two features observed in calorimetry was indeed associated with a nematic liquid crystalline mesophase. However, the situation was complicated by the growth of at least two and possibly three different crystal modifications at low temperature, with the relative quantities of the different phases depending on the cooling rate. Upon heating, these crystal phases melted at slightly different temperatures. Consistent with this observation,

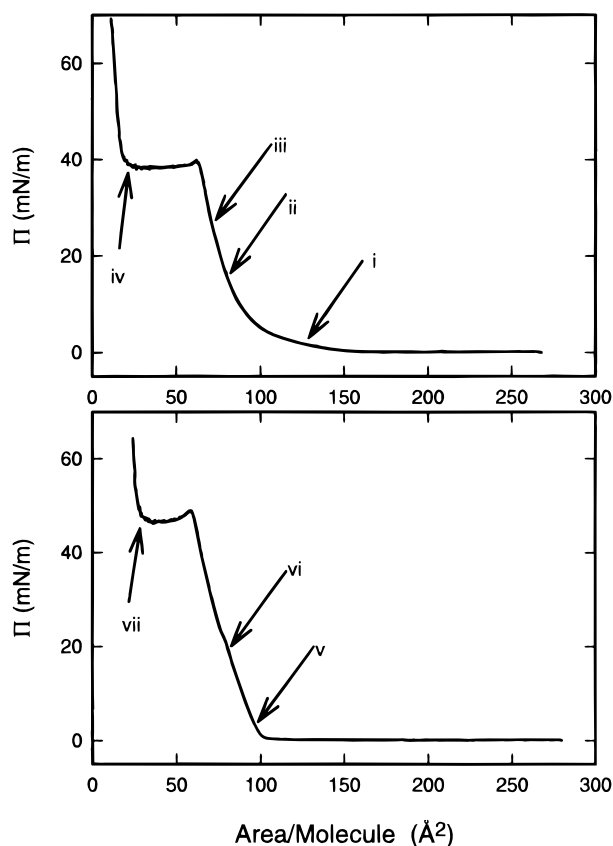


Figure 3. Pressure–area isotherms of **1** (top) and **2** (bottom) at the air–water interface. Arrows show points along the isotherms at which X-ray reflectivity profiles were measured.

we found that the detailed shape of the DSC traces, and the integrated enthalpy change under each peak, depended on the thermal history of the sample.

In **2** we observed a single broad endotherm (possibly with some internal structure) on heating, exhibiting an onset at 465 K and an enthalpy change of 64 J/g. Two exotherms were observed upon cooling. Optical microscopy confirmed that the region between the two exotherms corresponded to a monotropic nematic liquid crystalline phase.

Typical pressure–area isotherms for **1** and **2** at the air–water interface, measured on compression, are presented in Figure 3. Molecular areas at the beginning of the rapid rise were on the order of 100 Å² in both cases. If the barrier was stopped before reaching the plateau, the pressure remained constant to better than 10%. If the barrier was stopped on the horizontal plateau, the pressure for both samples was observed to drop to around 25 mN/m and then stabilize. Thus, we believe that the vertical rise is an equilibrium feature, while the behavior for areas less than 60 Å²/molecule is indicative of nonequilibrium processes. Indeed, the pressure maximum observed in both samples at the right-hand side of the plateau is a clear indication of nonequilibrium behavior. Furthermore, we visually observed stripes on the trough for areas $A < 60$ Å²/molecule, indicating the formation of bi- or multilayers. We never observed the pressure rise previously reported^{13–18} in the vicinity of 240 Å².

In an XR measurement, the photon momentum transfer is perpendicular to the air–water interface, and the reflected X-ray intensity is determined by the Fourier transform of the gradient of the electron density perpendicular to the water surface. We followed the common practice^{1,25} of analyzing the XR data by modeling the electron density at the interface as a stack of N uniform slabs (boxes), each with a different electron density

ρ_i , thickness L_i , and roughness σ_i describing the interface between slabs i and $i + 1$. The reflectivity is then given, as a function of photon momentum transfer Q_z , by

$$\frac{R(Q_z)}{R_F(Q_z)} = \left| \sum_{i=1}^{N+1} \left(\frac{\rho_i - \rho_{i-1}}{\rho_0} \right) e^{-iQ'_z D_i} e^{-Q'^2_z \sigma_i^2 / 2} \right|^2 \quad (1)$$

$$Q'_z = \sqrt{Q_z^2 - q_c^2} \quad (2)$$

where Q'_z is the refraction-corrected wavevector, q_c is the critical wavevector below which the reflectivity is unity, $R(Q_z)/R_F(Q_z)$ is the measured reflectivity divided by the Fresnel reflectivity calculated for a perfectly sharp subphase interface, ρ_0 is the electron density of the subphase, $\rho_{N+1} \sim 0$ is the density of the air or He above the sample, and $D_i = \sum_{j=1}^i L_j$ is the distance from the water surface to the interface between layer i and layer $(i + 1)$ (i.e., $D_0 = 0$). Our general procedure for analyzing the data was to use as few adjustable parameters as possible, consistent with obtaining reasonable agreement between the model and data. Although the error bars in fitted parameters obtained from a particular model were sometimes quite tight, our general experience from fitting similar data sets^{10,21,23} has been that model-dependent uncertainties (observed, for example, in changing from a 1-box to a 2-box model) lead to systematic uncertainties in all fitted parameters on the order of 10%. For an N -box fit, the fitting parameters were the overall intensity (constrained, however, to lie within 10% of the measured incident photon flux), as well as a density and thickness for each layer. Except as noted below, the roughness terms σ_i were all constrained to be identical to the roughness of the water surface σ_0 induced by capillary waves. This was taken to be an adjustable parameter in the fits but always converged to a value in the physical reasonable range.

In our XR measurements we observe changes in the surface-normal structure of **1** with pressure (Figure 4). Data are shown normalized to the calculated Fresnel reflectivity R_F , at various surface pressures. The maximum in R/R_F is due to constructive interference between the subphase–monolayer and monolayer–air interfaces. The rapid decrease in R/R_F at larger Q_z shows that the density profile, averaged over the rough water surface, is smeared out over a length scale $\sigma \sim 3$ – 4 Å. Solid lines show the results of least-squares fits to the data, and the parameters obtained with these fits are presented in Table 1. At $\Pi = 2.7$ mN/m good agreement was obtained with a one-box model, while for higher pressures two-box models were required. We interpret the total thickness, $L_1 + L_2$, as the thickness of a Langmuir monolayer, and the need for two boxes as representing density variations within the layer. As the pressure is increased, the layer thickness gradually increases.

Good agreement was obtained between the calculated charge density of **1** (504 e[−]/molecule) and the electron densities deduced from experiment. From the measured molecular area A and fitted parameters we can calculate

$$N_e = A \sum_{i=1}^N \rho_i L_i \quad (3)$$

At $\Pi = 2.7$ mN/m the experimental value of 600 differs by 19% from the calculated value, but at higher pressures measured values lie in the range 527–537 e[−]/molecule, within 7% of the value predicted. The relative thicknesses of the two layers and the calculated charge densities are internally consistent if we

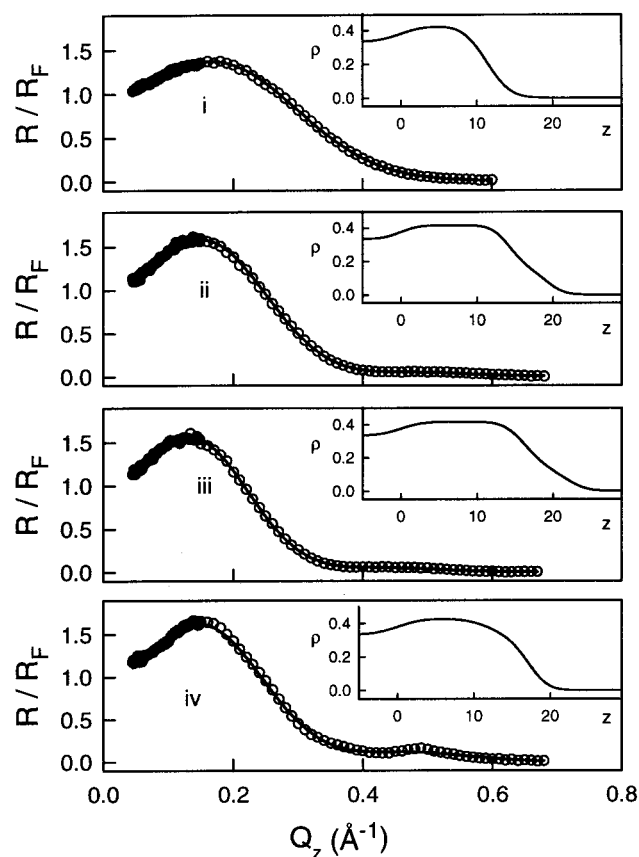


Figure 4. Reflectivity profiles (total reflectivity divided by Fresnel reflectivity) of **1** measured at points on the isotherm shown in Figure 3: (i) $\Pi = 3$ mN/m; (ii) $\Pi = 14.8$ mN/m; (iii) $\Pi = 27.0$ mN/m; (iv) full compression. Solid curves show fits to the data, as discussed in the text. The inset shows calculated electron density ρ ($\text{e}^-/\text{\AA}^3$) versus distance from the interface z .

TABLE 1: Results of Fits to X-ray Reflectivity Data^a

compd	Π (mN/m)	A (\AA^2)	ρ_1 ($\text{e}^-/\text{\AA}^3$)	L_1 (\AA)	ρ_2 ($\text{e}^-/\text{\AA}^3$)	L_2 (\AA)	σ (\AA)	N_e
1	2.7(5)	125	0.425	11.3			3.5	600
1	14.8(2)	80	0.416	14.3	0.159	4.8	2.7	537
1	27.0(5)	70	0.415	16.3	0.143	5.4	3.1	527
2	1.7(5)	95	0.439	15.0			3.3	626
2	19.2(2)	80	0.435	18.0			3.8	626

^a Π and A are the pressure and molecular area at which the measurement was made, obtained by correlating the measured pressure with the isotherms in Figure 3. L_i and ρ_i are the thickness and electron density of the first and second layers, σ is the Gaussian surface roughness, assumed for these fits to be the same for all interfaces, all obtained from least squares fits to the reflectivity data. The uncertainty in each of these parameters is on the order of 10%. N_e is the number of electrons per molecule calculated from the molecular area, layer thicknesses, and electron densities, to be compared with $N_e(\text{calcd}) = 504$ (for **1**) and 628 (for **2**).

associate the second layer with the last 3–4 carbons in the chains: 1.5 \AA per carbon yields $L_2 = 4.5 - 6.0$ \AA , and the calculated charge ratio is $\rho_2 L_2 / \rho_1 L_1 = 0.11 \rightarrow 0.15$, consistent with the ratios of 0.13 and 0.11 obtained from Table 1. In reality, of course, the charge density distribution must be more complicated, but our spatial resolution is limited to $\xi \sim \pi \text{\AA} / 0.7 \sim 5$ \AA by the range in Q_z provided by the XR measurements. Fine details of the structure may also be obscured by the roughness of the water subphase. The fact that the data are better modeled by a two-layer model simply reflects the general decrease in electron density from the bottom to the top of the film.

At the highest compression (point iv on the isotherm in Figure 3) we were unable to obtain a satisfactory fit to the reflectivity profile with any reasonable model. The solid line in Figure 4-iv shows the best fit to a two-box model, with $\rho_1 = 0.427$, $L_1 = 12.7$, $\rho_2 = 0.292$, $L_2 = 4.5$, and each layer allowed to have a different roughness σ_i . This model is inconsistent with the measured molecular charge and does not provide a good description of the maximum at $Q_z \sim 0.5 \text{\AA}^{-1}$. A four-box model corresponding to a 60 \AA film provides a better fit to the data, but with unphysical internal thicknesses. The most likely interpretation of the data is that we have coexistence of different layer thicknesses and that this coexistence cannot be represented by a simple slab model.

We now consider the molecular conformations of **1** that could give rise to the measured areas and reflectivity profiles. We used simple molecular modeling to obtain approximate dimensions of space-filling models starting from the configurations shown in Figure 1; calculated dimensions from these models are given in Table 2. If the entire molecule is parallel to the water, we obtain a molecular area of $310 \pm 60 \text{\AA}^2$ and a thickness of 5–7 \AA . No signature of such a structure was seen in either our Π – A isotherms or in XR. For the core and phenyl rings in contact with water, but alkyl chains projecting away from the interface, we obtain a molecular area of $205 \pm 35 \text{\AA}^2$ (depending in part on how the molecules are packed in two dimensions) and a thickness of 10 \AA , while if both chains (including both biphenyl and alkyl portions) project away from the interface the area and thickness are 72 \AA^2 and 21 \AA , respectively. We note that in this case the tails do not touch each other, so that the molecular area is determined by the core region in contact with the water. Finally, we can consider a structure intermediate between (a) and (c), such as that in Figure 1d, in which the tails are tilted an angle ϕ from the horizontal. For $0 < \phi < 90$ the molecular area could be as large as 310 \AA^2 , if the entire molecule is projected onto the surface, or as small as 70 \AA^2 , if we assume that the tails can arrange themselves as necessary to allow the cores to close-pack at the surface, and the layer thickness could range between 5 and 16 \AA .

If we compare these models with the XR and isotherm data, we see that the $\Pi = 2.7$ mN/m data are not consistent with any of the first three models. The most likely model is something similar to that in Figure 1d, with the tails neither touching the water surface nor completely vertical. A measured thickness of 11.3 \AA corresponds to $\phi = 23^\circ$. As the film is compressed, both the $\Pi = 14.8$ and $\Pi = 27.0$ data sets are consistent with either model 1c or 1d; i.e., the tails project away from the surface but are not necessarily normal to the surface. Thus the increase in film thickness with applied pressure suggests that the only structural change upon compression in this range is a continuous tilting of the tails toward a more vertical position.

Figure 5 shows the X-ray reflectivity from **2**, normalized to the calculated Fresnel reflectivity R_F . The results are generally similar to those obtained from measurements of **1**. For $\Pi = 1.7$ and 19 mN/m, good fits were obtained with a one-box model (with parameters given in Table 1). The data taken at full compression cannot be described with a one- or two-box model. The high frequency of the oscillations indicates that the film must be much thicker. Indeed, a good fit was obtained using a four-box model with a total thickness of 63 \AA , but with unphysical internal layer thicknesses. In any case, it seems clear that the nonequilibrium maximum observed in the isotherm, the pressure instability observed at small areas, and the visual

TABLE 2: Molecular Dimensions for Various Conformations of 1 and 2 Calculated from Simple Molecular Modeling (Chem 3D)^a

Compd	conformation	l (Å)	w (Å)	t (Å)	A (Å ²)
1	(a) parallel to water (Figure 1a)	52 ± 3	6 ± 1	6 ± 1	310 ± 60
1	(b) alkyl chains normal to water (Figure 1b)	34 ± 2	6 ± 1	10 ± 1	205 ± 35
1	(c) chains and phenyl rings normal to water (Figure 1c)	12 ± 1	6 ± 1	21 ± 2	70 ± 15
1	(d) tails tilted (Figure 1d)	$12 + 40 \cos \phi$	6 ± 1	$6 + 15 \sin \phi$	$70 + 240 \cos \phi$
2	(a) parallel to water (Figure 1a)	64 ± 3	6 ± 1	6 ± 1	385 ± 70
2	(b) alkyl chains normal to water (Figure 1b)	47 ± 2	6 ± 1	10 ± 1	280 ± 50
2	(c) chains and phenyl rings normal to water (Figure 1c)	12 ± 1	6 ± 1	28 ± 2	75 ± 15
2	(d) tails tilted (Figure 1d)	$12 + 52 \cos \phi$	6 ± 1	$6 + 22 \sin \phi$	$70 + 315 \cos \phi$

^a The corresponding schematic representations for **1** are given in Figure 1. The thickness t should be compared with the total film thickness $\sum_i L_i$ measured by XR measurements. The length l and width w are dimensions parallel to the surface, and their product is the area A , which should be compared with that obtained from Π - A isotherms.

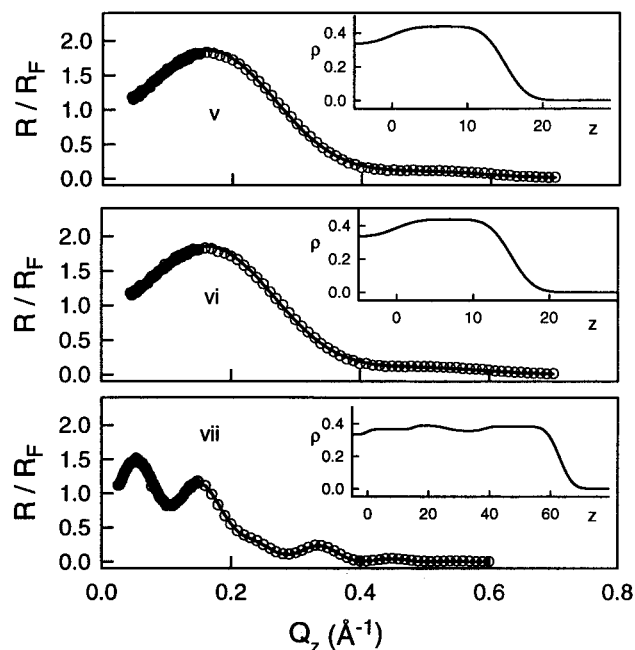


Figure 5. Reflectivity profiles (total reflectivity divided by Fresnel reflectivity) of **2** measured at points on the isotherm shown in Figure 5: (v) $\Pi = 2$ mN/m; (vi) $\Pi = 19$ mN/m; (vii) full compression. Solid curves show fits to the data. The inset shows calculated electron density ρ ($\text{e}^-/\text{\AA}^3$) versus distance from the interface z .

observation of stripes on the surface are all indicative of multilayer formation.

We can apply the same conformational analysis to the reflectivity data for **2** at $\Pi = 1.7$ and $\Pi = 19$ mN/m as that used above for **1**. The calculated molecular charges (Table 1) are fortuitously in extremely good agreement with the data. The areas and thicknesses calculated from molecular models similar to those in Figure 1 are given in Table 2. No evidence of a structure with the entire molecule in contact with water was seen in Π - A or XR measurements: the measured areas are too small and the measured thicknesses too large. Thicknesses of 15 and 18 Å measured from XR correspond to tilt angles (Figure 1d) of 26 and 34°, respectively, but these observations could also be described by some statistical combination of molecules exhibiting a range of tail tilts.

We now discuss our GID measurements, which probe the in-plane momentum transfer Q_{xy} . No features were seen in GID profiles of **1** at $\Pi = 2.7$, 14.8, or 27.0 mN/m. The most likely explanation is that the two-dimensional structure was fluid, or at least sufficiently disordered that no Bragg peaks were produced, although it is remotely possible that highly oriented crystallites were not detected in the single sample orientation at which measurements were made. Figure 6, top, shows GID

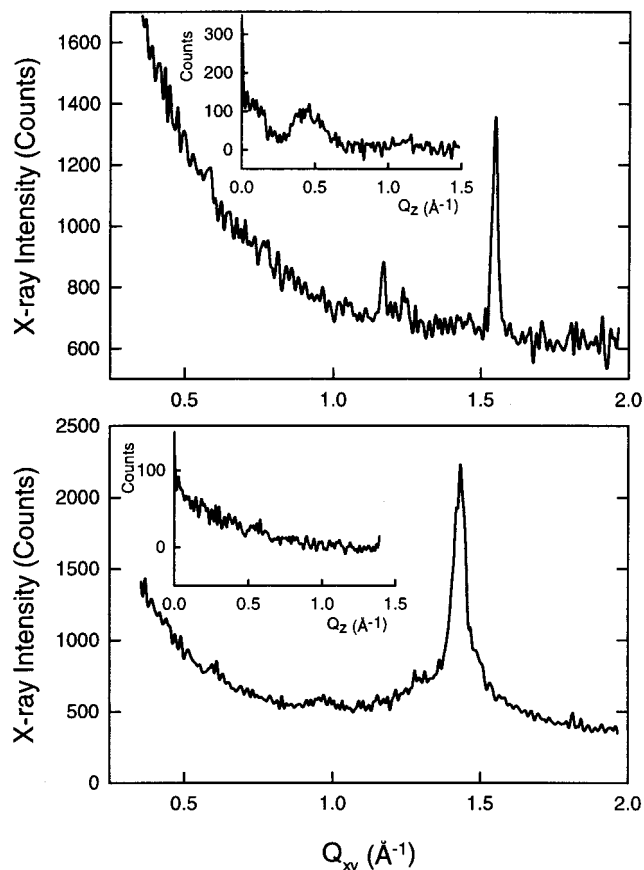


Figure 6. Top: GID profile from **1** at full compression (position iv in Figure 3). Points indicate the integrated X-ray counts (at 30 s/point) between $Q_z = 0$ and $Q_z = 0.5 \text{ \AA}^{-1}$ as a function of Q_{xy} . The inset shows the Q_z dependence of the intensity at $Q_{xy} = 1.51 \text{ \AA}^{-1}$, obtained by counting for 300 s at the peak position and subtracting the background intensity at $\pm 0.035 \text{ \AA}^{-1}$ from the peak. Bottom: GID profile from **2** at full compression (position vii in Figure 3). Points show Q_z -integrated intensity; the intensity shows the Q_{xy} dependence at $Q_{xy} = 1.39 \text{ \AA}^{-1}$ with the background intensity at $\pm 0.35 \text{ \AA}^{-1}$ subtracted.

of **1** at full compression, position (iv) in Figure 3. There is a strong feature at $Q_{xy} = 1.51 \text{ \AA}^{-1}$, corresponding to a spacing of 4.1 Å, together with several weaker features at smaller angles. A "Bragg rod" scan at $Q_{xy} = 1.51$ (inset) shows some structure up to $Q_z = 0.7 \text{ \AA}^{-1}$, consistent with thin-film diffraction. (The length scale of the film thickness is determined by the inverse of the Bragg rod length, $2\pi \text{ \AA}/0.7 \sim 9 \text{ \AA}$.) Keeping in mind that the XR data indicate the probable existence of multilayers, the precise structure cannot be determined. However, the most likely interpretation of the data is a crystalline mono- or multilayer structure. The unit cell might include one or several molecules, but the structure factor is dominated by chain-chain

interactions with a characteristic spacing of 4 Å. GID patterns of **1** at full compression were collected at several temperatures between 282 and 303 K, and no changes were observed, indicating that the film crystal structure is stable up to at least 303 K.

Similarly, the bottom panel of Figure 6 shows the GID profile of **2** at full compression. Again, a strong feature at 1.39 Å^{-1} ($d = 4.5 \text{ Å}$) indicates that the structure factor is dominated by interchain correlations. The Bragg rod has less structure but again extends to $\sim 0.7 \text{ Å}^{-1}$, consistent with thin film diffraction.

4. Conclusions

Our best model for the interfacial behavior of both **1** and **2** is the following: At high dilution the structure is unknown but most likely resembles the conformation in Figure 1d, with the tails projecting slightly away from the air–water interface (a small but nonzero value of ϕ). As the film is compressed, the tails are directed on the average farther and farther away from the interface, corresponding to larger values of ϕ or to a higher concentration of conformation (c) in statistical mixtures of (b), (c), and (d). This results in smaller molecular areas and thicker films. The molecular area changes by almost a factor of 2 in this process, corresponding to a high compressibility of the film. Within the film, the molecules are most likely fluid. When the molecular area is on the order of 70 Å^2 , the tails are all approximately vertical and packed as closely as possible within a monolayer, and at higher compression the film undergoes an irreversible collapse to a multilayer structure, which has, however, sufficient internal order to produce several Bragg peaks.

We observed no signs of a first-order lying-down to standing-up transition as reported by Wei *et al.*^{13–18} Although a definitive explanation for the difference in behaviors of our sample and theirs is at present unknown, it is highly likely that the crown ether liquid crystal samples prepared and studied by Wei *et al.* were contaminated with the same crown ether liquid crystal impurity **9** that we encountered in our initial syntheses.

Acknowledgment. We thank D. Vaknin, R. Composto, and J. K. Blasie for the use of their equipment. We thank D. Gidalevitz and B. M. Ocko for their assistance and for useful discussions. OYM, MRS, PAH, and ABS were supported by the MRSEC Program of the National Science Foundation (NSF) under Award No. DMR96-32598. Research was carried out in part at the National Synchrotron Light Source, Brookhaven National Laboratory, supported under U.S. DOE Contract No. DE-AC02-98CH10886.

References and Notes

- (1) Als-Nielsen, J.; Jacquemain, D.; Kjaer, K.; Leveiller, F.; Lahav, M.; Leiserowitz, L. *Phys. Rep.* **1994**, *246*, 251 and references therein.
- (2) Jacquemain, D.; Grayer Wolf, S.; Leveiller, F.; Deutsch, M.; Kjaer, K.; Als-Nielsen, J.; Lahav, M.; Leiserowitz, L. *Angew. Chem., Int. Ed. Engl.* **1992**, *31*, 130.
- (3) Durbin, M. K.; Malik, A.; Richter, A. G.; Yu, C. J.; Eisenhower, R.; Dutta, P. *Langmuir* **1998**, *14*, 899.
- (4) Lednev, I. K.; Petty, M. C. *Adv. Mater.* **1996**, *8*, 615 and references therein.
- (5) Lehn, J.-M. *Supramolecular Chemistry: Concepts and Perspectives*; VCH: Weinheim, 1995.
- (6) Malthete, J. J.; Poupinet, D.; Vilanove, R.; Lehn, J.-M. *J. Chem. Soc. Chem. Commun.* **1989**, 1016.
- (7) Mertesdorf, C.; Ringsdorf, H. *Liq. Cryst.* **1989**, *5*, 1757.
- (8) Maliszewskyj, N. C.; Heiney, P. A.; Blasie, J. K.; McCauley, J. P., Jr.; Smith, A. B., III. *J. Phys. II* **1992**, *2*, 75.
- (9) Heiney, P. A.; Gidalevitz, D.; Maliszewskyj, N. C.; Satija, S.; Vaknin, D.; Pan, D.; Ford, W. T. *Chem. Commun.* **1998**, 1483.
- (10) Gidalevitz, D.; Mindyuk, O. Y.; Stetzer, M. R.; Heiney, P. A.; Kurnaz, M. L.; Schwartz, D. K.; Ocko, B. M.; McCauley, J. P., Jr.; Smith, A. B., III. *J. Phys. Chem. B* **1998**, *102*, 6688.
- (11) El Abed, A. M.; Peretti, P.; Gallet, F.; Billard, J. *J. Phys. II Fr.* **1993**, *3*, 851.
- (12) El Abed, A. M.; Daillant, J.; Peretti, P. *Langmuir* **1993**, *9*, 3111.
- (13) Fang, J. Y.; Lu, Z.-H.; Pan, S. P.; Chen, Z. L.; Wei, Y.; Qin, J.; Xie, M. C. *Solid State Commun.* **1992**, *82*, 1023.
- (14) Zhu, Y. M.; Lu, Z.-H.; Jia, X. B.; Wei, Q. H.; Xiao, D.; Wei, Y.; Wu, Z. H.; Hu, Z. L.; Xie, M. G. *Phys. Rev. Lett.* **1994**, *72*, 2573.
- (15) Zhu, Y.-M.; Wei, Y. *J. Chem. Phys.* **1994**, *101*, 10023.
- (16) Zhu, Y. M.; Lu, Z. H.; Wei, Y. *Phys. Rev. E* **1995**, *51*, 418.
- (17) Dong, X.; Yang, X. M.; Zhu, Y. M.; Lu, Z. H.; Wei, Y. *Thin Solid Films* **1994**, *251*, 40.
- (18) Zhu, Y. M.; Jia, X. B.; Xiao, D.; Lu, Z. H.; Wei, Y.; Wu, Z. H.; Hu, Z. L.; Xie, M. G. *Phys. Lett. A* **1994**, *188*, 287.
- (19) Xie, M. G.; Qin, J.; Hong, F.; Wang, L. *Mol. Cryst. Liq. Cryst.* **1991**, *209*, 309.
- (20) Kricheldorf, H. R.; Kaschig, J. *Liebigs Ann. Chem.* **1976**, 882.
- (21) Gidalevitz, D.; Mindyuk, O. Y.; Heiney, P. A.; Ocko, B. M.; Henderson, P.; Ringsdorf, H.; Boden, N.; Bushby, R. J.; Martin, P. S.; Stzalka, J.; McCauley, J. P., Jr.; Smith, A. B., III. *J. Phys. Chem. B* **1997**, *101*, 10870.
- (22) **Materials and Methods:** All reactions were carried out in oven-dried glassware under an argon atmosphere, unless otherwise noted. All solvents were reagent grade. Tetrahydrofuran (THF) was freshly distilled from sodium/benzophenone under argon before use. Dichloromethane and benzene were freshly distilled from calcium hydride before use. Triethylamine was distilled from calcium hydride and stored over potassium hydroxide. Unless stated otherwise, all reactions were magnetically stirred and monitored by thin layer chromatography using 0.25 mm Whatman precoated silica gel plates. Flash column chromatography was performed with the indicated solvents using silica gel-60 (particle size 0.023–0.040 mm) supplied by E. Merck.
- (23) Gidalevitz, D.; Mindyuk, O. Y.; Heiney, P. A.; Ocko, B. M.; Kurnaz, M. L.; Schwartz, D. K. *Langmuir* **1998**, *14*, 2910.
- (24) Ocko, B. M.; Wu, X. Z.; Sirota, E. B.; Sinha, S. K.; Gang, O.; Deutsch, M. *Phys. Rev. E* **1997**, *55*, 3164 and references therein.
- (25) Tidswell, I. M.; Ocko, B. M.; Pershan, P. S.; Wasserman, S. R.; Whitesides, G. M.; Axe, J. D. *Phys. Rev. B* **1990**, *41*, 1111.